Chapter 4
Supported Nickel Nanocatalysts for the Dry Reforming of Methane: Effect of SBA-15's Pore Sizes on the Catalytic Performances of Nickel Nanoparticles

Oscar Daoura, Maya Boutros, Marie-Nour Kaydouh, Pascale Massiani, Franck Launay, and Nissrine El Hassan

4.1 Introduction

Catalysts made of transition metal (e.g., Ni, Co, Fe, Cu…) nanoparticles (NPs) have a wide range of applications such as in hydrogenation, hydrogenolysis or hydrodeoxygenation reactions; they can also be used in processes targeting the production of renewable energy resources such as the Fischer-Tropsch (FT) synthesis or the methane reforming and water–gas shift reaction [1–3]. In methane reforming, the size and consequently the dispersion of the involved metals play a key role in catalytic performances [4, 5]. As it is well-known, metallic particles with nanometric dimensions exhibit interesting physicochemical characteristics and usually, their catalytic activity is inversely proportional to their size [6]. Several oxide supports (alumina, silica, etc) have been tested in order to improve the dispersion of the active phase. Among them, siliceous carriers offer valuable features including their high surface areas, tunable nanoscale pore dimensions and sizes, variable accessible morphologies, and their rather low price [7–10]. However, due to diffusion limitation

O. Daoura
Laboratoire de Chimie Physique des Matériaux, LCPM/PR2N, Lebanese University, Faculty of Sciences II, Jdeideh, Lebanon

Laboratoire de Réactivité de Surface, LRS, Sorbonne Université, CNRS, Paris, France

M. Boutros
Laboratoire de Chimie Physique des Matériaux, LCPM/PR2N, Lebanese University, Faculty of Sciences II, Jdeideh, Lebanon

M.-N. Kaydouh · N. El Hassan (✉)
Department of Chemical Engineering, Faculty of Engineering, University of Balamand, Amioun El Koura, Lebanon
e-mail: nissrine.hassan@balamand.edu.lb

P. Massiani · F. Launay (✉)
Laboratoire de Réactivité de Surface, LRS, Sorbonne Université, CNRS, Paris, France
e-mail: franck.launay@sorbonne-universite.fr

M. Piumetti, S. Bensaid (eds.), *Nanostructured Catalysts for Environmental Applications*, https://doi.org/10.1007/978-3-030-58934-9_4

of the metallic precursors throughout the pore channels during the preparation step, the resulting metal nanoparticles are often not only dispersed inside the pores but also located on the outer surface of the grains, giving rise to aggregation. Moreover, examples of partial or even total loss of metallic active surface have been revealed during high temperature catalyst activation and/or operation as the result of NPs growth by migration, coalescence, and Ostwald ripening [11, 12].

SBA-15 type supports prepared by a self-assembly $(S^0H^+)(X^-I^+)$ pathway (where S^0 stands for a neutral Surfactant (Pluronic P123), I^+ for cationic inorganic silica species, H^+ for protons, and X^- for chloride) are characterized by a two-dimensional hexagonal pore structure, a narrow pore size distribution, large specific surface area, and a rather high thermal stability (larger walls than MCM-41) [13, 14]. For these reasons, they are often considered as suitable carriers for the immobilization of metal NPs, especially nickel, affording notably heterogeneous catalysts for the dry reforming of methane (DRM) [15]. This reaction that consumes simultaneously methane and carbon dioxide to produce H_2 and CO (Eq. 4.1) in an equimolar ratio presents undoubtedly environmental and industrial interests.

$$CH_4 + CO_2 \rightarrow 2H_2 + 2CO \tag{4.1}$$

Indeed, it allows the conversion of two greenhouse gases into syngas with a H_2/CO ratio suitable for the Fischer-Tropsch synthesis (FTS) [15]. Owing to their good activity and the lower price of Ni compared to noble metals, Ni nanoparticles are preferred for DRM [16]. However, due to the endothermic nature of the reaction (high temperatures are needed in order to reach acceptable conversions) and to the existence of side reactions such as methane decomposition (Eq. 4.2) and Boudouard reaction (Eq. 4.3), nickel nanoparticles are suffering from sintering and coke deposition [17].

$$CH_4 \rightarrow 2H_2 + C_{(s)} \tag{4.2}$$

$$2CO \rightarrow CO_2 + C_{(s)} \tag{4.3}$$

In addition, the reverse water gas shift reaction (Eq. 4.4) can also take place, which leads to selectivity issues since it consumes the H_2 produced by the DRM process and generates more CO [18].

$$CO_2 + H_2 \rightarrow H_2O + CO \tag{4.4}$$

To improve their stability, the nickel nanoparticles can be deposited into the confined space of the pore channels of the SBA-15 support [18] whose diameter should play a key role, even though such effect was, to our knowledge, not specifically analyzed before. Hence, our target in the present work was to better understand confinement effects in SBA-15 and more precisely the impact of the pore sizes on the nickel nanoparticles incorporation in the channels, on their sizes, and on Ni

dispersion. The "Two-Solvents" (TS) impregnation up 5 wt.% of nickel was applied on commercially available SBA-15 supports with 4, 5, and 7 nm pore diameters. The activities of those new catalysts were tested in the DRM reaction.

4.2 Experimental Part

4.2.1 Materials Preparation

Three commercially available SBA-15 supports (Sigma-Aldrich, CAS Number: 7631-86-9, ref.: 806803-5G, 806862-5G, 806854-5G) having different mean pore diameters (4, 5, and 7 nm), referred as S4, S5, and S7, respectively, were investigated here. Nickel (5 wt%) was incorporated by a postsynthesis method from an aqueous solution of $Ni(NO_3)_2.6H_2O$ affording Ni/S4, Ni/S5, and Ni/S7 samples. In details, the TS method used [19] consisted in suspending 1 g of the support in 35 mL of pentane (Sigma-Aldrich), then adding drop wise a volume of water equal to the silica pore volume (determined by N_2 physisorption and chosen in order to ensure a complete confinement of the Ni active phase in the pores of the support) and containing the appropriate amount of nickel precursor (0.25 g of $Ni(NO_3)_2.6H_2O$) (Sigma-Aldrich). The resulting solids were dried for three days at room temperature, then overnight at 60 °C, and they were finally calcined in air in an oven (static conditions) at 550 °C for 5 h (heating rate 1 °C min^{-1}).

4.2.2 Characterizations

Textural properties were determined from N_2 adsorption-desorption isotherms recorded on a Belsorp-max (MicrotracBEL) apparatus. Before measurements, the samples were degassed under vacuum for 2 h at 250 °C on BelprepII-vac. Specific surface areas were obtained using the BET equation. The mean pore diameters and specific pore volumes were determined using the BJH model.

X-ray Diffraction (XRD) data were recorded in the 2θ range between 5 and 90° on a Bruker D8 diffractometer apparatus using the Cu Kα radiation (λ = 1.5405 Å), 30 kV, and 10 mA conditions, a step size of 0.04° and 4 s per step. The average nickel particle size, D, for each sample was calculated (when possible) from the Scherrer equation (Eq. 4.5).

$$D = K\lambda / \beta\cos\theta \tag{4.5}$$

where K is a constant (K = 0.9), λ = 1.5405 Å, β is the full width at half maximum (FWHM) of the diffraction peak, and θ is the peak position.

Thermogravimetric analyses (TGA) were performed in order to quantify the carbon deposits on 10 mg of the spent catalysts using a TA SDT Q600 thermal analyzer

instrument. Measurements were carried out from room temperature to 900 °C (heating rate 10 °C min^{-1}) under flowing air (100 mL min^{-1}).

Temperature Programmed Reduction (TPR), carried out on an Autochem 2910 (Micromeritics) apparatus equipped with a thermal conductivity detector, was used in order to study the nickel reducibility (on calcined materials). The samples (80 mg) were heated in a U-shaped quartz sample tube from room temperature to 800 °C at a rate of 10 °C min^{-1} using 5 vol% H_2/Ar (25 mL min^{-1}). A bath of isopropanol and liquid N_2 was used before the TCD detector in order to trap the water formed during NiO reduction. In addition, the nickel percentage (wt.%) was calculated from the quantitative H_2 consumption evaluated by integrating the reduction peak assuming the following reaction (Eq. 4.6)

$$NiO + H_2 \rightarrow Ni + H_2O \tag{4.6}$$

An Autochem 2910 apparatus was also used to perform reductions mimicking the in-situ reduction (detailed later, see Sect. 4.2.3) carried out before the catalytic test.

Transmission Electron Microscopy (TEM) analyses were performed on a JEOL-2020 (LaB) microscope operating at 200 kV. Prior to each measurement, the sample powder was embedded in a polymer matrix that was cut using an ultramicrotome, then slices were deposited on a copper grid coated with a porous carbon film. Hence, the observations made at room temperature could be done from the core to the surface of the grains of catalysts.

H_2 Chemisorption experiments were performed on a BELSORB-max equipment from BEL JAPAN. The samples (about 200 mg) were reduced in-situ under a flow of H_2 (50 mL min^{-1}) at 650 °C for 2 h using a ramp of 10 °C min^{-1}. The sample was then outgassed at 620 °C for 2 h under vacuum (about 5.10^{-1} Pa). A first, H_2 chemisorption was performed at 25 °C, the pressure at equilibrium being recorded when the pressure variation was below 0.02% per min. The sample was then outgassed for 2 h at 25 °C before a second H_2 chemisorption was done under the same conditions as above. Nickel particle size estimations were based on a truncated octahedron geometry, assuming a complete reduction, semispherical particles, and a H/Ni adsorption stoichiometry factor of 1. The experimental data were fitted with a Langmuir adsorption equation (Eq. 4.7) and the amount of surface nickel was calculated from the quantity adsorbed at saturation (Q_{max} in the model). The dispersion thus refers here to the molar percentage of surface Ni atoms compared to the total number of Ni atoms in the sample.

$$\theta = \frac{Q_{ads}}{Q_{max}} = \frac{\sqrt{KP}}{1 + \sqrt{KP}} \tag{4.7}$$

θ: Fractional occupancy of the adsorption sites, Q_{ads}: Quantity adsorbed, Q_{max}: Quantity adsorbed on saturation, K: Equilibrium constant, P: Partial pressure of the adsorbate.

4.2.3 Catalytic Measurements

The catalysts were tested with a PID ENG & TECH Microactivity Effi Reactor. About 50 mg of powdered calcined material was loaded into the reactor (on quartz wool) and reduced in-situ at 650 °C for 2 h (10 °C min^{-1}) in a 5% H_2/Ar flow (30 mL min^{-1}) in order to ensure a complete conversion of nickel oxide into metallic nickel. After this pretreatment step, the temperature was decreased to 200 °C and the test of dry reforming of methane was started. This was conducted under atmospheric pressure, using a reactants ratio CH_4/CO_2 of 1:1 (each reactant being diluted at 10% in Ar) with a total flow of 60 mL min^{-1} (Gas Hourly Space Velocity (GHSV) = 72 L g^{-1} h^{-1}). The activity of the catalyst was measured by first increasing the temperature from 200 °C up to 650 °C (5 °C min^{-1}), then maintaining the temperature at 650 °C for 12 h for stability measurements. The gaseous products were analyzed online by an Agilent 490 micro-GC equipped with Plot-U (for the detection of CO_2) and molecular sieves (for the detection of H_2, CH_4, and CO) channels, and a thermal conductivity detector (TCD). The conversions of methane and carbon dioxide were calculated according to Eqs. (4.8) and (4.9), respectively, and the H_2/CO ratios were estimated using Eq. (4.10):

$$\mathrm{CH_4\ conversion}, \% = \frac{\left(\mathrm{CH_{4(in)}} - \mathrm{CH_{4(out)}}\right)}{\mathrm{CH_{4(in)}}} \times 100 \tag{4.8}$$

$$\mathrm{CO_2\ conversion}, \% = \frac{\left(\mathrm{CO_{2(in)}} - \mathrm{CO_{2(out)}}\right)}{\mathrm{CO_{2(in)}}} \times 100 \tag{4.9}$$

$$\mathrm{H_2 / CO} = \frac{\mathrm{H_{2(out)}}}{\mathrm{CO_{(out)}}} \tag{4.10}$$

4.3 Results and Discussion

4.3.1 Physicochemical Characterizations of the Supports and Calcined Ni-based SBA-15 Materials

Figure 4.1 displays the nitrogen adsorption-desorption isotherms of the supports (as purchased) and of the corresponding impregnated samples. The corresponding textural parameters are listed in Table 4.1.

According to the IUPAC classification, the isotherms of the supports as well as their corresponding Ni-based solids are of type IV (a), in good agreement with what

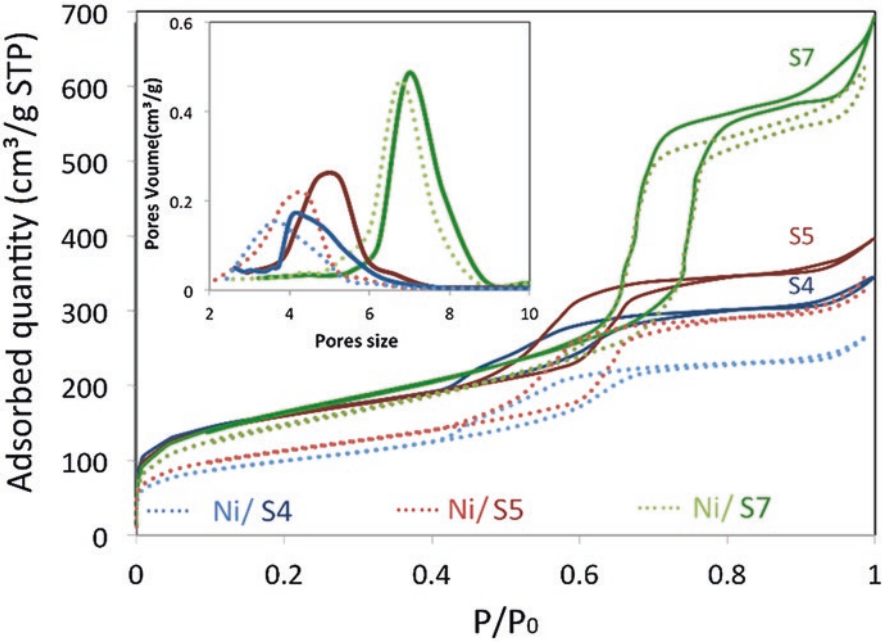

Fig. 4.1 N_2 adsorption-desorption isotherms at −196 °C and pores size distributions of the calcined Ni/S4, Ni/S5, and Ni/S7 materials and of their corresponding supports

Table 4.1 Textural properties of Ni/S materials

Materials	S_{BET} $m^2\ g^{-1}$	V_{Pores} [a] $cm^3\ g^{-1}$	$D_{Pores\ des.}$ [b] (nm)
S4	573	0.42	4.0
Ni/S4	357	0.37	3.5
S5	571	0.64	5.0
Ni/S5	412	0.55	4.4
S7	593	1.02	7.0
Ni/S7	537	0.98	6.9

[a] Pores volume and [b] pores size estimated by BJH method from the desorption branch

is expected for mesoporous materials of the SBA-15 type [20], but with some variations between the samples.

The three supports (S4, S5, and S7) are characterized by very similar specific surface area of ~580 $m^2\ g^{-1}$ (Table 4.1). The value decreased after nickel impregnation by 37%, 28%, and 11% for Ni/S4, Ni/S5, and Ni/S7, respectively (Table 4.1). The pore volumes of the S4, S5, and S7 supports decreased as well after nickel impregnation by 0.05 (−12%), 0.09 (−14%), and 0.05 (−4%) $cm^3\ g^{-1}$, respectively (the weight of the support without nickel being taken into consideration). From those results, it can be emphasized that, whatever the carrier considered, the decrease of the pore volume was more important than expected assuming the incorporation

of all Ni in the pores (5 wt.% and using a density of 8.9 g cm^{-3} for Ni(0)). This was specifically the case on the S4 and S5 supports, suggesting that total or partial pore blocking has occurred after nickel impregnation on these two supports. Such observation is in good agreement with the decrease of the mean pores diameter also observed for both S4- and S5-based materials after their impregnation and with their plugged hysteresis loops revealed by N_2 sorption in the P/P_0 region between 0.4 and 0.5 (Fig. 4.1).

The hystereses observed for S4 and S5 solids before and after impregnation are close to that of H5 type (especially for S4 solids), revealing the presence of both open and partially blocked mesopores (e.g., plugged hexagonal templated silicas) [20]. On the other hand, the S7 adsorption-desorption isotherms form an H1 hysteresis loop typical of well-organized hexagonal mesopores with a narrow pore size distribution (typical for SBA-15).

4.3.2 Catalytic Activity

The performances of the in-situ reduced samples toward the DRM reaction were evaluated in terms of CH_4 and CO_2 conversions under a GHSV of 72 L g^{-1} h^{-1}. The CH_4 and CO_2 conversions at $t = 0$ and after 12 h are presented in Fig. 4.2 as a function of the mean pores sizes in the catalyst. The three materials exhibited good catalytic performances, with conversions of both CH_4 and CO_2 close to those expected at thermodynamic equilibrium ones. Nevertheless, it can be seen that the activity tends to be improved while increasing the pores diameter of the SBA-15 support. Thus, Ni/S7 led to the highest conversion values of CH_4 and CO_2 (77% and 80%, respectively) and the deactivation after 12 h of catalytic test was the lowest (decrease

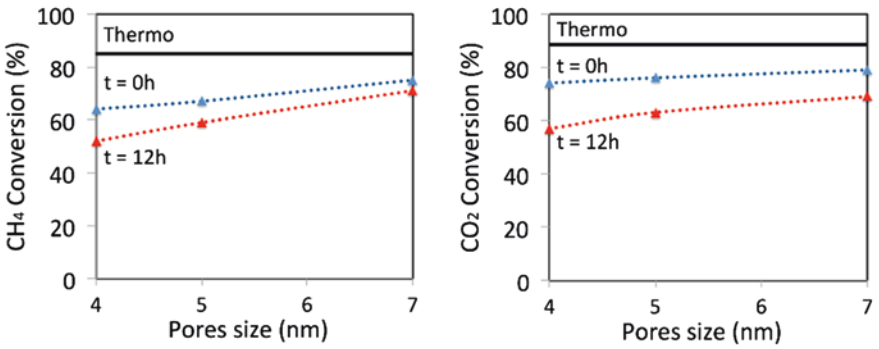

Fig. 4.2 Reactant conversions on the Ni-based SBA-15 catalysts at $t = 0$ (blue curve) and $t = 12$ h (orange curve) under a GHSV of 72 L g^{-1} h^{-1} (corresponding to a total flow of 60 mL min^{-1} and 50 mg of catalysts) as a function of the mean pores size of the supports; thermodynamic equilibrium values (black) calculated from the HSC (7.1) software (at 1 atm with an inlet feed ratio of $CO_2/CH_4 = 1$ and assuming no carbon formation occurring during the reaction) are also represented for comparison

of only 2% and 6% for CH_4 and CO_2, respectively). In contrast, Ni/S4 gave rise to the lowest conversion values (50% and 57%) and the highest deactivation after 12 h (decrease of 6% and 11% for CH_4 and CO_2, respectively).

In order to better understand those differences, a deeper investigation of the characteristics of the nickel-based species will be performed in the following part considering the Ni/S_4 and Ni/S7 samples having the smallest and largest pores of the series, respectively.

4.3.3 NiO and Ni^0 Characterization

The first difference which could be clearly emphasized between the two solids arose from their nickel oxide reduction behavior.

The TPR profiles displayed in Fig. 4.3 show that the Ni/S4 and Ni/S7 samples are characterized by a "two-step" reduction profile. The H_2 consumption at lower temperature (375 °C) is usually attributed to the reduction of bulk NiO with low metal-support interaction and/or big aggregates [21]. Such component of the reduction profile was the major one in the case of Ni/S4. On the other hand, the second peak (centered at 455 or 510 °C for Ni/S4 and Ni/S7, respectively) can be tentatively assigned to the reduction of NiO species strongly interacting with the SiO_2 surface. From those results, we can clearly conclude that the Ni/S7 solid exhibits a more important fraction of nickel in good interaction with the support. Such strong Ni-support interaction should enhance the stability of nickel nanoparticles in the catalysts and hence contribute to the higher catalytic stability seen above for Ni/S7, thus confirming the crucial role of metal-support interaction in the stabilization of

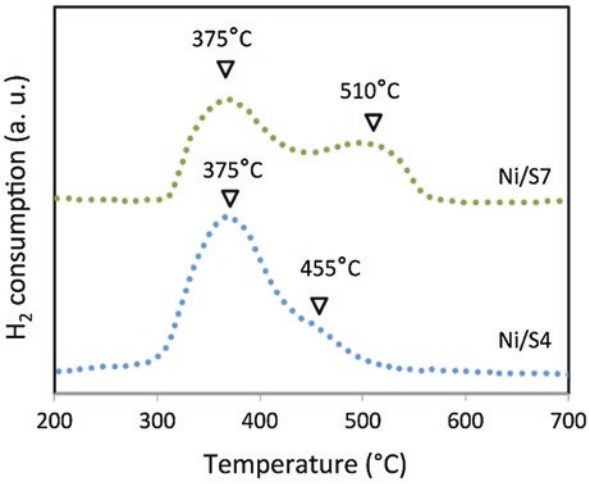

Fig. 4.3 H_2-TPR profiles of calcined Ni/S4 and Ni/S7 samples recorded with a H_2 5 Vol.%/Ar flow of 30 mL min^{-1} and a heating rate of 10 °C min^{-1}

Ni nanocatalysts [22, 23]. Last but not least, it is also important to note that the Ni wt.% estimated from the H_2 consumption during TPR analysis was 4.2 wt.% for both samples, which is close to the expected value of 5 wt.%.

The XRD patterns of the calcined and reduced Ni/S4 and Ni/S7 samples (Fig. 4.4) show a main wide peak in the 15° < 2θ°< 30° range typical of X-rays diffusion phenomena in amorphous silica walls. In addition, five intense diffraction peaks at 2θ° = 37.2°, 43.3°, 62.9°, 75.4°, and 77° corresponding to face-centered cubic lattice (Fm-3m) nickel oxide (JCPDS no. 89-7130) are observed for the calcined solids. After reduction under conditions very similar to those used just before the catalytic test (2 h at 650 °C), these peaks are substituted by three other ones at 2θ° = 44°, 52°, and 76°, characteristic of the face-centered cubic lattice (Fm-3m) of metallic Ni^0 (JCPDS no. 70-1849). The NiO particles sizes estimated from Scherrer equation (Eq. 4.5) were 7 nm and 5.4 nm for calcined Ni/S4 and Ni/S7, respectively (Table 4.2). In Ni/S7, this corresponds to a mean NiO size value smaller than the mean pores diameter of the S7 support, which would indicate that some particle size control by the pores occurred in this case. However, this was not the case for the S4-based material since the nickel oxide particles in Ni/S4 turned out to be larger than the pores size of S4. Such conclusions are in good agreement with above TPR data suggesting the presence of weakly interacting big NiO particles and with N_2 sorption results indicating some hindrance to pores access. Surprisingly, it is noteworthy that the XRD experiments performed after Ni/S4 and Ni/S7 reduction did not allow to show significant differences between NiO and Ni^0 particle size (Table 4.2).

In line with XRD results, clear differences between the two reduced solids were revealed by TEM analyses (Fig. 4.5).

In both cases, relatively good nickel dispersions could be emphasized from TEM images. However, some big Ni^0 aggregates were revealed on the external surface of the grains in the case of Ni/S4. Indeed, the particle sizes distribution extended

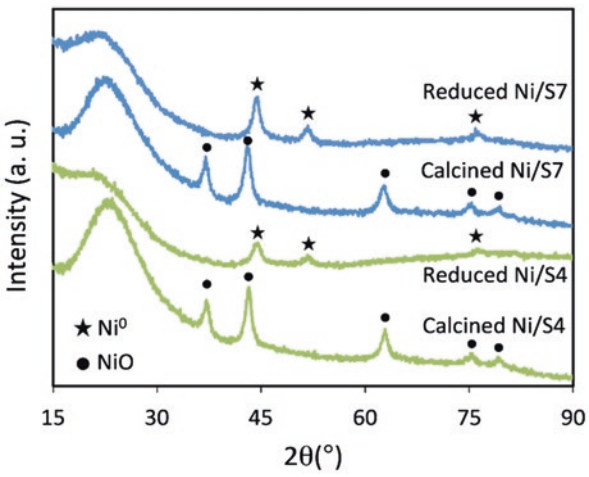

Fig. 4.4 XRD patterns of Ni/S4 and Ni/S7 samples after calcination or reduction (at 650 °C for 2 h (10 °C min^{-1}) in a 5% H_2/Ar flow (30 mL min^{-1}))

Table 4.2 H_2 chemisorption analysis at 20 °C after in-situ reduction under H_2 flow at 650 °C and nickel crystal size estimated from several methods for reduced and spent Ni/S materials

Materials	NiO size (nm)[a]	Ni^0 size (nm)[b]	Ni^0 size (nm)[c]	Ni dispersion (%)	Ni surface area ($m^2\ g^{-1}$)	Ni^0 size (nm) [d]	Ni^0 size (nm) [e]
Ni/S4	7.0	7.2	7.4	7.8	2.2	12	7.2
Ni/S7	5.4	5.1	5.8	11.6	3.2	8.7	5.8

Estimated from XRD results for [a] calcined and, [b] reduced solids; [c] Estimated from TEM images of the reduced solids; [d] Estimated from H_2 chemisorption; [e] Estimated from XRD results for spent solids

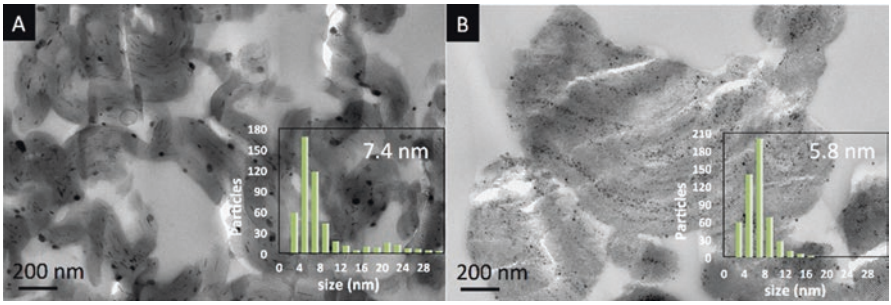

Fig. 4.5 TEM images of reduced A: Ni/S4 and B: Ni/S7 samples

towards 20–24 nm for Ni/S4 (Fig. 4.5a). This was not the case for the counts performed on the images of Ni/S7 (Fig. 4.5b), which reflects again, in good correlation with TPR results, a better incorporation and confinement of Ni in the pores of S7. In addition, the mean Ni particles size (reduced samples) estimated from the TEM images (on 400–500 particles) was 5.8 vs. 7.4 nm for Ni/S7 and Ni/S4, respectively. Such values are also in good agreement with the conclusion made from the discussion of the XRD results that emphasized indirectly a more successful confinement/incorporation effect for the support with the largest pores size (S7).

In this work, an attempt of Ni dispersion measurement was proposed by following the method described by Bartholomew and coworkers on the basis of the first H_2 isotherm (including reversibly and irreversibly chemisorbed hydrogen) [24]. H_2 chemisorption results (Table 4.2) emphasized the higher metal dispersion (and smaller nickel particles) in Ni/S7 compared to Ni/S4. These results are again in good agreement with the trends revealed by TEM and XRD, demonstrating further that Ni/S7 is characterized by smaller particles and better Ni dispersion. However, the greater Ni particles size estimated by H_2 chemisorption compared with those deduced from XRD and TEM may result from the weak bonding of hydrogen on some Ni sites or some difficulties in the accessibility of hydrogen to part of the Ni sites.

4.3.4 Spent Solids Characterization

After the catalytic test, the spent Ni/S catalysts were examined using TGA, XRD, and TEM in order to monitor the eventual modifications in their nickel dispersion as well as coke deposition, which could occur due to the side reactions. TGA analysis of the spent Ni/S catalysts (Fig. 4.6a) emphasizes the presence of carbon deposits of similar nature for both samples. The quantity of carbon was however, twice more for Ni/S4 compared to Ni/S7, being around 6 wt.%, which is however a value that remains below the quantities reported for other catalysts [25, 26]. The result for Ni/S7 is in good correlation with the stronger deactivation tendency exhibited by this catalyst during the DRM test (Fig. 4.2). Such observation also points out the excellent sintering resistance of nickel particles detected in majority inside the pores of S7. Indeed, it is well-known that the coke deposition is more favorable on big nickel aggregates [27]. In addition, no nanotubes were detected on the TEM images of Ni/S7 where all the nickel was incorporated in the porosity. In that case, the Ni^0 nanoparticles turned out to be still embedded into the porosity of S7 and no large

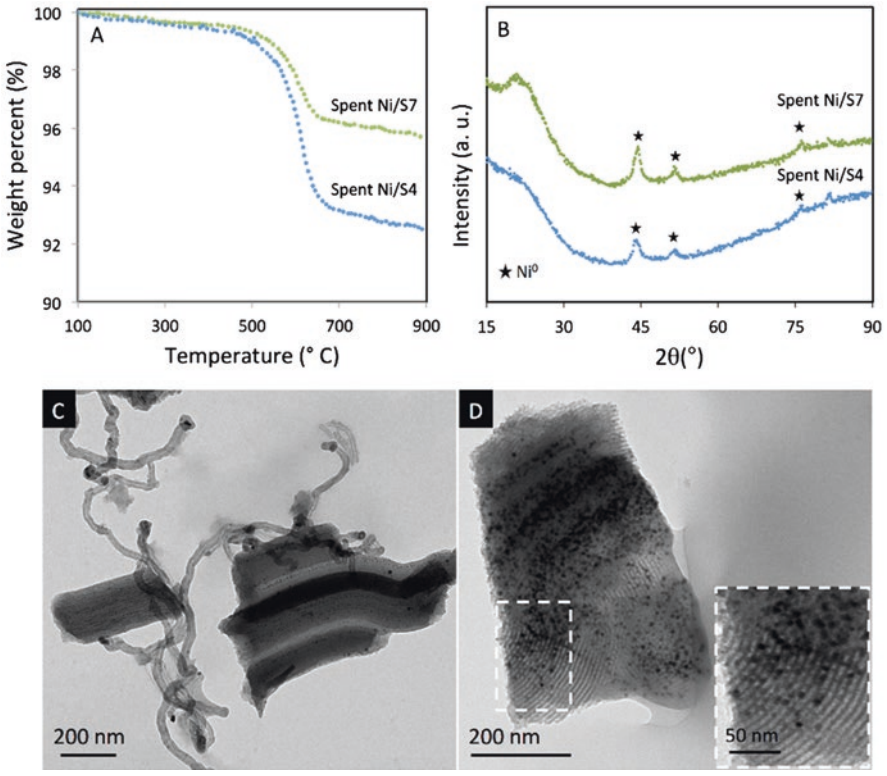

Fig. 4.6 (**a**) TGA profiles and (**b**) XRD patterns of spent Ni/S4 and Ni/S7 samples. (**c**, **d**) TEM images of spent Ni/S4 and Ni/S7 samples, respectively

nickel particles could be highlighted (Fig. 4.6d). It appears clearly that the big Ni aggregates detected on the external surface of the grains in the case of Ni/S4 (Fig. 4.6c) were less resistant to coke deposition contrary to those of Ni/S7. However, it is good to know that in the case of Ni/S7, carbon nanotubes were observed on some of the nickel particles, in minority, detected outside the grains. XRD results for both spent samples (Fig. 4.6b) exhibited three peaks corresponding to face centered cubic lattice of Ni^0 at $2\theta = 44°$, 52°, and 76° (JCPDS no. 70-1849) with no significant sintering (7.2 nm vs. 5.8 nm for Ni/S4 and Ni/S7, respectively) or carbon detected (due to the low quantity or to the presence of non ordered carbon that can be detected from TGA as well).

4.4 Conclusion

A systematic study of the effect of the size of pores in SBA-15 supports on the performances of nickel-SBA-15 catalysts in DRM reaction was carried out. N_2 sorption results obtained on the series of three catalysts with similar metal loading (4.2 wt.%) clearly emphasize the impact of the pore diameter on the incorporation of nickel inside the channels. Thus, pore plugging occurred in the case of S4 and S5 with smaller channel diameters, but not in S7 having the largest pores size. XRD, TEM, and H_2 sorption analysis also pointed out differences related to the mean Ni/NiO particles size that was smaller (~5 nm vs. ~7 nm) and related to a higher metal dispersion (11.6% vs. 7.8%) when the support with the largest pores (S7) was considered. TPR of Ni/S7 also highlighted a better metal-support interaction than in Ni/S4 as reflected by the presence of a reduction peak at higher temperature (around 550 °C) while most of NiO is reduced below 450 °C in Ni/S4. Based on these results, we can conclude that the better catalytic performances achieved on reduced Ni/S7 result from an easier access to porosity of the Ni precursor during the impregnation step, leading to better Ni dispersion. On the contrary, some Ni remained at the exterior of the SBA-15 grains in Ni/S4, giving bigger Ni-based nanoparticles poorly attached to the support and strongly sensitive to sintering. Such result looks like others reported in the literature. Indeed, in 2015, T. Shimizu and coworkers [28] demonstrated that Rh particles (4 wt.%) included in a mesoporous MCM-41 support used for hydrogenation of cinnamaldehyde tend to migrate out easily and to agglomerate on the external surface of the support during calcination, whereas those prepared in a mesostructured silica with larger pores size (MSU-H) remained quite unchanged. In addition, Yuan and coworkers [29] have shown that, for ordered hexagonal mesostructure ((Mo-Ni)-silica based catalysts with 13 wt.% of Mo and 3 wt.% of Ni), a support with a larger mean pore size gives rise to higher hydrodesulfurization performance efficiency. Also, Song and coworkers [30] who studied the pores size effect of siliceous supports on the performances of cobalt (15 wt.%) for the FT reaction demonstrated that the catalysts with pores diameter of about 6–10 nm displayed higher activity and good C5+ selectivity compared to those with smaller pores.

Acknowledgments This work was supported by the ANR (France) and CNRS-L (Lebanon) national agencies through their respective funding provided in the frame of the ERANETMED EU-FP7 initiative (Energy-065 SOL-CARE project, JC-ENERGY-2014 first call). The authors would like also to thank Dr. C. Thomas from LRS for the interpretation of the H_2 chemisorption experiments.

References

1. S. Chakraborty, H. Dai, P. Bhattacharya, N. Fairweather, M. Gibson, J. Krause, H. Guan, Iron-based catalysts for the hydrogenation of esters to alcohols. J. Am. Chem. Soc. **136**, 7869–7872 (2014)
2. K. Mallikarjuna, C. Bathula, K. Buruga, N. Shrestha, Y.Y. Noh, H. Kim, Green synthesis of palladium nanoparticles using fenugreek tea and their catalytic applications in organic reactions. Mater. Lett. **205**, 138–141 (2017)
3. H.Y. Zhao, D. Li, P. Bui, S.T. Oyama, Hydrodeoxygenation of guaiacol as model compound for pyrolysis oil on transition metal phosphide hydroprocessing catalysts. Appl. Catal. A Gen. **391**, 305–310 (2011)
4. H. Drobna, M. Kout, A. Sołtysek, V. González-Delacruz, A. Caballero, L. Capek, Analysis of Ni species formed on zeolites, mesoporous silica and alumina supports and their catalytic behavior in the dry reforming of methane. React. Kinet. Mech. Catal. **121**, 255–274 (2017)
5. X.Y. Gao, J. Ashok, S. Widjaja, K. Hidajat, S. Kawi, Ni/SiO_2 catalyst prepared via Ni-aliphatic amine compelxation for dry reforming of methane: effect of carbon chain number and amine concentration. Appl. Catal. A Gen. **503**, 34–42 (2017)
6. J. Woo Han, J.S. Park, M. Suk Choi, H. Lee, Uncoupling the size and support effects of Ni catalysts for dry reforming of methane. Appl. Catal. B Environ. **203**, 625–632 (2017)
7. X. Chen, S. Wang, J. Zhuang, M. Qiao, K. Fan, H. He, Mesoporous silica-supported NiB amorphous alloy catalysts for selective hydrogenation of 2-ethylanthraquinone. J. Catal. **227**, 419–427 (2004)
8. X. Yang, D. Chen, S. Liao, H. Song, Z. Li, Z. Fu, Y. Su, High-performance Pd-Au bimetallic catalyst with mesoporous silica nanoparticles as support and its catalysis of cinnamaldehyde hydrogenation. J. Catal. **291**, 36–43 (2012)
9. A.K. Prashar, S. Mayadevi, P.R. Rajamohanan, N. Devi, In situ encapsulation of Pt nanoparticles in mesoporous silica: synthesis, characterisation and effect of particle size on CO oxidation. Appl. Catal. A Gen. **403**, 91–97 (2011)
10. V. Gutiérrez, F. Nador, G. Radivoy, M.A. Volpe, Highly selective copper nanoparticles for the hydrogenation of α,β-unsaturated aldehydes in liquid phase. Appl. Catal. A Gen. **464-465**, 109–115 (2013)
11. T.W. Hansen, A.T. Delariva, S.R. Challa, A. Datye, Sintering of catalytic nanoparticles: particle migration or Ostwald ripening? Acc. Chem. Res. **46**, 1720–1730 (2013)
12. P. Munnik, P.E. de Jongh, K.P. de Jong, Recent developments in the synthesis of supported catalysts. Chem. Rev. **115**, 6687–6718 (2015)
13. L. Karam, S. Casale, H. Zakhem, N. El Hassan, Tuning the properties of nickel nanoparticles inside SBA-15 mesopores for enhanced stability in methane reforming. J. CO_2 Utiliz. **17**, 119–124 (2017)
14. M.N. Kaydouh, N. El Hassan, A. Davidson, S. Casale, H. El Zakhem, P. Massiani, Effect of the order of Ni and Ce addition in SBA-15 on the activity in dry reforming of methane. C. R. Chim. **18**, 293–301 (2015)
15. M.N. Kaydouh, *Nickel confinement effect into mesoporous silica supports based catalysts for the syngas production via the dry reforming of methane*. Dissertation, Sorbonne Université (2016)

16. O. Daoura, S. Daher, M.N. Kaydouh, N. El Hassan, P. Massiani, F. Launay, M. Boutros, Influence of the swelling agents of siliceous mesocellular foams on the performances of Ni-based methane dry reforming catalysts. Int. J. Hydrog. Energy **43**, 17205–17215 (2018)
17. O. Daoura, M.N. Kaydouh, N. El Hassan, P. Massiani, F. Launay, M. Boutros, Mesocellular silica foam-based Ni catalysts for dry reforming of CH_4 (by CO_2). J. CO_2 Utiliz. **24**, 112–119 (2018)
18. O. Daoura, G. El Chawich, M. Boutros, N. El Hassan, P. Massiani, O. Ersen, W. Baaziz, F. Launay, Aqueous nickel(II) hydroxycarbonate instead of nickel(0) colloids as precursors of stable Ni-silica based catalysts for the dry reforming of methane. Catal. Commun. **138**, 105953–105957 (2020)
19. J. Van der Meer, I. Bardez-Giboire, C. Mercier, B. Revel, A. Davidson, R. Denoyel, Mechanism of metal oxide nanoparticle loading in SBA-15 by the double solvent technique. J. Phys. Chem. C **114**, 3507–3515 (2010)
20. M. Thommes, K. Kaneko, A.V. Neimark, J. Oliver, F. Rodriguez-Reinoso, J. Rouquerol, K. Sing, Physisorption of gases, with special reference to the evaluation of surface area and pore size distribution (IUPAC Technical Report). Pure Appl. Chem., 1051–1060 (2015)
21. M.J.F.M. Verhaak, A.J. van Dillen, J.W. Geus, Measuring the acid-base properties of supported nickel catalysts using temperature-programmed desorption of ammonia. Appl. Catal. A Gen. **105**, 251–269 (1993)
22. Z. Taherian, M. Yousefpour, M. Tajally, B. Khoshandam, A comparative study of ZrO_2, Y_2O_3 and Sm_2O_3 promoted Ni/SBA-15 catalysts for evaluation of CO_2/methane reforming performance. Int. J. Hydrog. Energy **42**, 16408–16420 (2017)
23. S. Kawi, Y. Kathiraser, J. Ni, U. Oemar, Z. Li, T. Saw, Progress in synthesis of highly active and stable nickel-based catalysts for carbon dioxide reforming of methane. ChemSusChem **8**, 3556–3575 (2015)
24. C.H. Bartholomew, Hydrogen adsorption on supported cobalt, iron, and nickel. Catal. Lett. **7**, 27–51 (1990)
25. A. Albarazi, M.E. Gálvez, P. Da Costa, Synthesis strategies of ceria–zirconia doped Ni/SBA-15 catalysts for methane dry reforming. Catal. Commun. **59**, 108–112 (2015)
26. Z. Taherian, M. Yousefpour, M. Tajally, B. Khoshandam, Catalytic performance of Samaria-promoted Ni and Co/SBA-15 catalysts for dry reforming of methane. Int. J. Hydrog. Energy **42**, 24811–24822 (2017)
27. S. Arora, R. Prasad, An overview on dry reforming of methane: strategies to reduce carbonaceous deactivation of catalysts. RSC Adv. **6**, 108668–108688 (2016)
28. T. Shimizu, M. Ota, Y. Sato, H. Inomata, Effect of pore structure on catalytic properties of mesoporous silica supported rhodium catalysts for the hydrogenation of cinnamaldehyde. Chem. Eng. Res. Des. **104**, 174–179 (2015)
29. P. Yuan, J. Liu, Y. Li, Y. Fan, G. Shi, H. Liu, X. Bao, Effect of pore diameter and structure of mesoporous sieve supported catalysts on hydrodesulfurization performance. Chem. Eng. Sci. **111**, 381–389 (2014)
30. D. Song, J. Li, Effect of catalyst pore size on the catalytic performance of silica supported cobalt Fischer–Tropsch catalysts. J. Mol. Catal. A Chem. **247**, 206–212 (2006)